Open Archive TOULOUSE Archive Ouverte (OATAO)

OATAO is an open access repository that collects the work of Toulouse researchers and makes it freely available over the web where possible.

To link this article: http://dx.doi.org/10.1007/s11214-016-0310-z

CrossMark

Seismic Coupling of Short-Period Wind Noise Through Mars' Regolith for NASA's InSight Lander

N.A. Teanby[1] · J. Stevanović[1,2] · J. Wookey[1] ·
N. Murdoch[3] · J. Hurley[4] · R. Myhill[1] · N.E. Bowles[5] ·
S.B. Calcutt[5] · W.T. Pike[6]

Abstract NASA's InSight lander will deploy a tripod-mounted seismometer package onto the surface of Mars in late 2018. Mars is expected to have lower seismic activity than the Earth, so minimisation of environmental seismic noise will be critical for maximising observations of seismicity and scientific return from the mission. Therefore, the seismometers will be protected by a Wind and Thermal Shield (WTS), also mounted on a tripod. Nevertheless, wind impinging on the WTS will cause vibration noise, which will be transmitted to the seismometers through the regolith (soil). Here we use a 1:1-scale model of the seismometer and WTS, combined with field testing at two analogue sites in Iceland, to determine the transfer coefficient between the two tripods and quantify the proportion of WTS vibration noise transmitted through the regolith to the seismometers. The analogue sites had median grain sizes in the range 0.3–1.0 mm, surface densities of 1.3–1.8 g cm^{-3}, and an effective regolith Young's modulus of $2.5^{+1.9}_{-1.4}$ MPa. At a seismic frequency of 5 Hz the measured transfer coefficients had values of 0.02–0.04 for the vertical component and 0.01–0.02 for the horizontal component. These values are 3–6 times lower than predicted by elastic theory and imply that at short periods the regolith displays significant anelastic behaviour. This will result in reduced short-period wind noise and increased signal-to-noise. We predict the noise induced by turbulent aerodynamic lift on the WTS at 5 Hz to be $\sim 2 \times 10^{-10}$ ms^{-2} Hz$^{-1/2}$

✉ N.A. Teanby
n.teanby@bristol.ac.uk

[1] School of Earth Sciences, University of Bristol, Wills Memorial Building, Queens Road, Bristol, BS8 1RJ, UK

[2] Present address: AWE Blacknest, Brimpton, Reading, RG7 4RS, UK

[3] ISAE-SUPAERO, DEOS/Systèmes Spatiaux, 10 avenue Edouard Belin, BP 54032, 31055 Toulouse, France

[4] STFC Rutherford Appleton Laboratory, Harwell Science and Innovation Campus, Didcot OX11 0QX, UK

[5] Atmospheric, Oceanic, & Planetary Physics, University of Oxford, Clarendon Laboratory, Parks Road, Oxford OX1 3PU, UK

[6] Department of Electrical and Electronic Engineering, Imperial College, London SW7 2AZ, UK

🙲 Springer

with a factor of 10 uncertainty. This is at least an order of magnitude lower than the InSight short-period seismometer noise floor of 10^{-8} ms^{-2} Hz$^{-1/2}$.

**Keywords** Mars · Seismology · Geophysics

1 Introduction

NASA's Interior Exploration using Seismic Investigations, Geodesy and Heat Transport (InSight) mission will be the first dedicated geophysics mission to Mars. InSight launches in May 2018 and, after a short cruise phase, will land in November 2018. The mission goal is to probe the near surface and deep internal structure of Mars in detail for the first time (Banerdt et al. 2012, 2013; Lognonne et al. 2015). A major component of the mission is the Seismic Experiment for Interior Structure (SEIS) instrument (Mimoun et al. 2012), which comprises two three-component seismometers; the Very Broad Band (VBB) seismometer (Lognonne et al. 2014; Dandonneau et al. 2013) and the Short-Period (SP) seismometer (Pike et al. 2005; Delahunty and Pike 2014), both mounted on a tripod levelling system. SEIS-VBB is most sensitive to frequencies from 0.01–1 Hz and SEIS-SP is most sensitive to frequencies from 0.1–10 Hz. The instruments are predicted to have similar noise levels at ~ 2 Hz. SEIS will be deployed onto Mars' surface using a robot arm to ensure the best possible surface coupling and best chance of detecting marsquakes and other seismic signals.

There are expected to be two major sources of seismic signal on Mars: faulting due to release of stress in the crust as Mars' interior cools (Golombek et al. 1992; Knapmeyer et al. 2006; Roberts et al. 2012; Taylor et al. 2013); and meteorite impacts (Davis 1993; Teanby and Wookey 2011; Teanby 2015). These studies predict that Mars will be less seismically active than the Earth by approximately two orders of magnitude (Knapmeyer et al. 2006; Panning 2016). This is offset by the expectation of lower ambient noise on Mars compared to Earth (Lognonne et al. 1996; Mimoun et al. 2016) due to lack of vegetation, ocean waves, or anthropogenic activity. The main seismic noise source at long-periods is expected to be ground tilting caused by the time-varying atmospheric pressure field. At shorter periods, wind is also expected to be an important noise source, especially during periods of strong surface wind such as dusk, dawn, and global dust storms. Wind noise could couple directly into a surface-exposed seismometer or indirectly via vibrations induced in near-by lander components such as InSight's solar panels (Murdoch et al. 2016a). Mars' surface also experiences extreme temperature variations due to its thin atmosphere, with day-night excursions reaching over 80 K at the equator. On Earth seismic deployments are usually buried to provide a stable thermal environment and prevent direct wind coupling with the seismometer. On Mars burying the seismometer is too technologically challenging at present, so to provide a stable thermal environment protected from the wind the SEIS instrument will be covered by a wind and thermal shield (WTS), lowered over the instrument by the robot arm. Figure 1 illustrates the SEIS deployment sequence and operational surface layout.

While the seismometers will be protected from the direct effects of wind by the WTS, wind gusts and flow instabilities will induce movements in the WTS, which will be transferred though the martian regolith (soil layer) to the seismometers inside. In this paper we quantify the seismic transfer coefficient between the WTS and SEIS so that noise estimates can be made. We use a field-based experimental approach, with a 1:1-scale simplified model of the WTS and SEIS tripods on an analogue martian surface. The regolith transfer coefficient was measured at a frequency of ~ 5 Hz, which allowed lightweight commercial geophones to be used. This frequency is close to the ~ 2 Hz cross-over in performance between

Fig. 1 The InSight lander SEIS and WTS deployment sequence. (**a**) Initially both SEIS and WTS are mounted on the lander deck. (**b**) The robot arm deploys SEIS to the surface. (**c**) Robot arm positions the WTS over SEIS and (**d**) finally lowers the WTS to cover SEIS. (**e**) Cross section showing the inner SEIS experiment tripod and outer WTS tripod. The WTS has a flexible chainmail skirt to improve the seal with the ground. Images (**a**–**d**) courtesy of NASA/JPL-Caltech
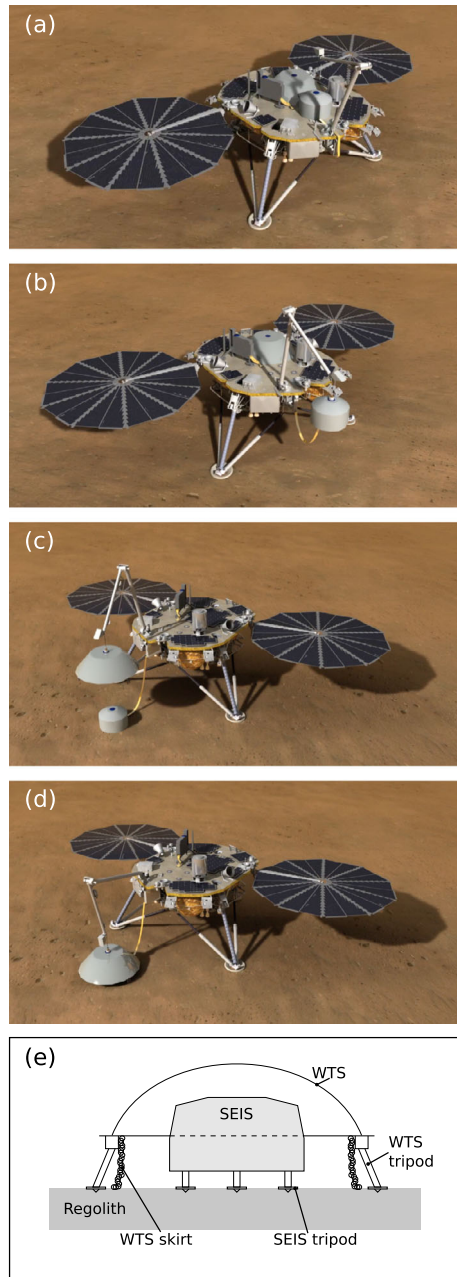
SEIS-VBB and SEIS-SP. Our aims are to: (1) quantify the regolith WTS-to-SEIS noise transfer coefficient; (2) determine if this differs from simple elastic model predictions; and (3) determine if there is an optimum alignment of the inner SEIS tripod relative to the outer WTS tripod for minimisation of wind noise. For context, the complete InSight noise model, which includes all instrumental and environmental sources, is summarised by Mimoun et al.
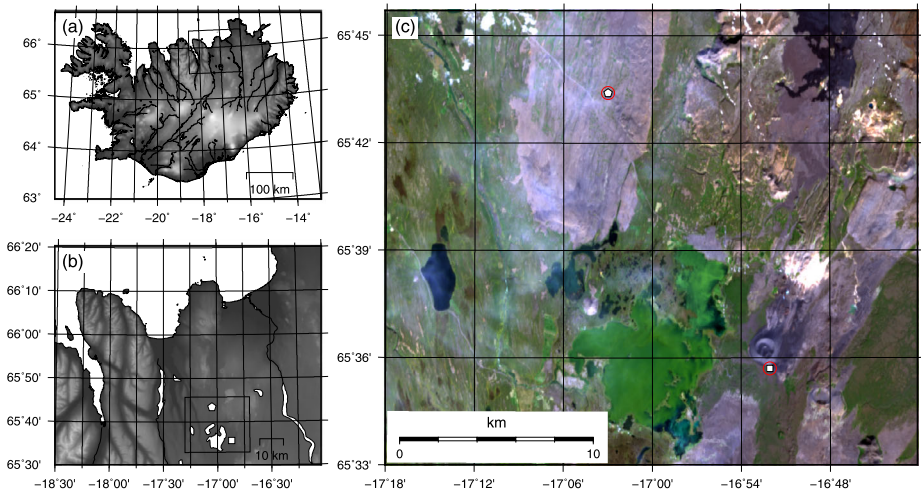
Fig. 2 Field site locations. (**a**, **b**) Shaded relief maps showing general location of the sites in northeast Iceland. (**c**) Location of field sites marked on Landsat 8 georegistered false-colour image acquired 28th August 2014 (*red band* B4 640–670 nm, *green band* B3 530–590 nm, and *blue band* B2 450–510 nm). The Hverfjall site is located at 16°52′04″ W, 65°35′42″ N (*white square*) and the Holasandur site is located at 17°03′01″ W, 65°43′24″ N (*white pentagon*)

(2016) and Murdoch et al. (2016a,b). These studies cover the 0.01–1 Hz bandwidth assuming an elastic regolith, whereas our study focuses on higher frequency and anelastic effects.

2 Field Sites

Our field experiments were carried out in northeast Iceland, which has many cold deserts of fine grained basaltic material, little vegetation or soil to hold moisture, and relatively arid conditions (Arnalds et al. 2001). For this reason northeast Iceland is often used as a Mars analogue (Greeley et al. 2002; Hartmann et al. 2003). Figure 2 shows the locations of our two field sites, which were close to the town of Reykjahlið and Lake Mývatn. The first site was just south of Hverfjall tephra crater (Mattsson and Höskuldsson 2011) on the apron at the base of the crater (16°52′04″ W, 65°35′42″ N). The second site was in Holasandur (Arnalds et al. 2001), a black sand desert just north of highway 87 (17°03′01″ W, 65°43′24″ N). These sites were chosen for lack of vegetation and well drained fine-grained surface conditions. Figure 3 shows photographs of the sites.

Samples of the surface material were taken at depths of 0 cm and 10 cm at each site so that densities and grain size distributions could be determined. Densities were determined from 100–200 gramme bulk samples using a measuring cylinder and micro-balance. The Hverfjall site had densities of 1.3 ± 0.1 g cm^{-3} for the surface layer and 1.5 ± 0.1 g cm^{-3} at 10 cm depth, whereas the Holasandur site had densities of 1.8 ± 0.1 g cm^{-3} at the surface and 1.7 ± 0.1 g cm^{-3} at 10 cm depth.

Grain size distributions were determined by sieving ten 50 gramme samples for each depth from each site and are shown in Fig. 4. At both sites the upper surface layer is coarser grained due to removal of fines by the wind. This is typical of desert sites and has also been observed in scoop images from the Mars rovers (Arvidson et al. 2004; Lorenz and
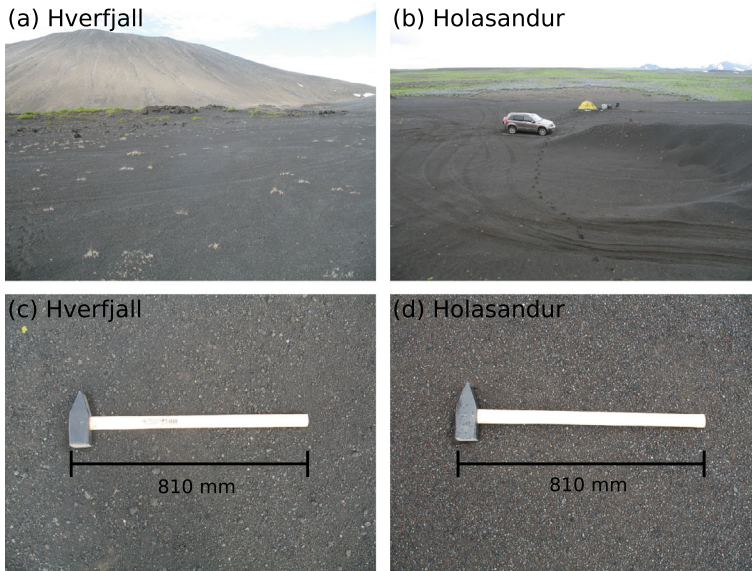
Fig. 3 Field site photographs. (**a**) Hverfjall site looking north towards the main tephra crater. (**b**) Holasandur site looking northwest. Both sites were chosen for their lack of vegetation and fine-grained surface material. (**c, d**) Close ups of surface texture with a sledge hammer for scale

Fig. 4 Grain size distributions from the field sites determined using graded sieving. Surface and 10 cm depth samples were measured for each site, showing that the surface is coarser grained. Also shown in the median (0.5) position is a histogram of median grain sizes measured by the Spirit Mars Exploration Rover (Cabrol et al. 2014). Our field sites have a grain size distribution in broad agreement with the Mars data
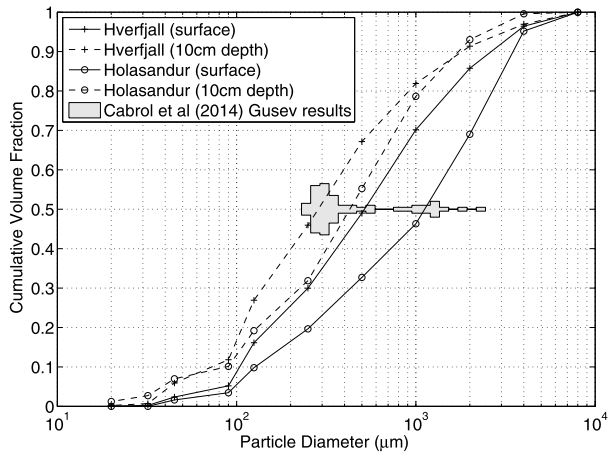
Zimbelman 2014). Also shown in the figure is a histogram of the median grain size distribution measured by the microscopic imager on the Mars exploration rover Spirit (Cabrol et al. 2014) during its drive around Gusev crater. The Spirit results are consistent with other in-situ measurements, which show a significant fine grained component (Christensen and Moore 1992; Barlow 2008; Pike et al. 2011), and remote sensing data that also indicate fine-grained surface cover over much of Mars (Ruff and Christensen 2002). The median grain size at our site (i.e. where the cumulative distribution function is equal to 0.5) overlaps with the Spirit Gusev results and provides a reasonable analogue to a typical martian surface, with the Hverfjall site being the closest match.

Fig. 5 Experimental equipment setup. (**a**) The outer tripod represents the WTS tripod and is topped by a tetrahedron frame with a central mechanical noise source to represent vibrations of the WTS by the wind. A 4.5 Hz SM6 geophone is mounted at the left vertex close to a tripod foot. The inner tripod represents the SEIS experiment and has an identical central 4.5 Hz geophone. (**b**) Inner and outer tripod in clocked orientation. (**c**) Inner and outer tripod in anti-clocked orientation. (**d**) Details of foot design, which includes a central 45° tapered spike surrounded by a 60 mm radius disc to limit sinking
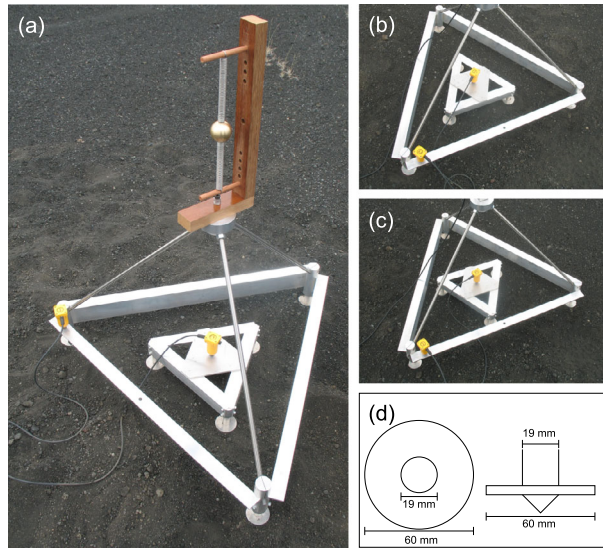
3 Method

To measure the wind noise coupling transfer coefficient at each field site we constructed a simplified 1:1-scale replica of the SEIS tripod and WTS tripods from 3 mm thick aluminium angle-sections, shown in Fig. 5. The inner tripod has a side length of 0.30 m and the outer tripod had a side length of 0.80 m. The foot design was similar to InSight's, with a 60 mm diameter anti-sink disc surrounding a 19 mm diameter shaft with a 45° tapered spike. The current best estimates of the InSight flight masses are 9.5 kg for the WTS (outer tripod) and 8.2 kg for the SEIS instrument package (inner tripod). Mars' gravity is 3.71 ms^{-2} compared to 9.81 ms^{-2} on Earth. Therefore, to maintain similar effective weights to the actual flight hardware, our scale replicas required lower masses. This could be important as increased weight compresses the surface grains more and could alter their combined elastic properties. The mass of our tripods were 7.4 kg for the outer tripod and 1.7 kg for the inner tripod. These masses were designed around an earlier specification, which had a heavier WTS and a lighter SEIS package, but remain within a factor of two of the Mars-equivalent weights of the current flight hardware. Field tests using a range of tripod masses show that this mass difference is likely to affect the measured transfer coefficients by less than 5 % (Taylor 2014), which is negligible compared to other experimental error sources.

Wind vibrations of the WTS were simulated using a mechanical noise source connected to the outer tripod at the apex of a tetrahedron mounted on the tripod. We tried three different noise sources: a solenoid impulse generator; an unbalanced motor with reduction gearing; and a 463 gramme brass sphere on a double spring. The solenoid impulse generator was poor at generating low frequencies in the seismic range of interest (< 10 Hz) and mostly created high frequency (∼ 100 Hz) ringing of the outer tripod and tetrahedron struts. The unbalanced motor had a very small signal at low frequencies and the motor reduction gear mechanism created excessive noise. The mass on a double spring was by far the best source: the double spring gave a stable oscillation with a single frequency and could be used to generate vertical or horizontal vibrations. The double spring was pre-tensioned to give a smooth motion in both vertical and horizontal directions.

The seismic signals generated by the spring on the outer tripod, and measured at the inner tripod after passing through the soil/regolith, were measured by ION Geophysical SM6 4.5 Hz vertical or horizontal geophones with a sensitivity of 20 V/ms^{-1} at 5 Hz. These geophones had the advantage of being lightweight—0.17 kg for the verticals and 0.22 kg for the horizontals—so did not add much extra weight to the inner tripod or unbalance the outer tripod. The inner tripod geophone was mounted in the centre of the tripod on a stiff 6 mm thick aluminium plate. The outer tripod geophone was mounted close to one of the three tripod feet. Symmetry of the tetrahedron meant that this was representative of the signal generated at each foot. The mass of the brass sphere and spring stiffnesses were chosen such that the double spring source had a resonant frequency close to 4.5 Hz. This ensured maximum signal-to-noise for a frequency close to the crossover in performance of the SEIS-VBB and SEIS-SP.

Seismic signals were recorded on a National Instruments 6210 USB 16bit 8 channel data logger. The NI6210 is not a field ruggedised instrument so we enclosed it in an IP68 rated moisture and dust resistant enclosure. This enclosure also provided additional electrical shielding. A field laptop powered by a car battery and power inverter running NI SignalExpress was used to control the datalogger and record the data. The NI6210 had a selectable input voltage range of ± 0.2, ± 1, ± 5, or ± 10 V. The smallest ± 0.2 V range was used to obtain the best bit resolution. The NI6210 analogue to digital converter (ADC) input operates as an 8 channel multiplexer, so to avoid spurious signals or cross talk caused by residual voltages at the multiplexer input we logged four channels such that geophone inputs were followed by an empty channel with a grounded input. Data were logged at 5 kHz to allow identification of any high frequency spurious signals.

The experimental procedure at each site was as follows:

– Position tripods with either the inner and outer tripods aligned (Fig. 5b) or anti-aligned (Fig. 5c), referred to as "clocked" and "anti-clocked" respectively.
– Prime the brass sphere by extending in the vertical or horizontal direction, depending on type of geophones installed.
– Start logging data and release the mass after a pause of one or two seconds.
– Record 30 seconds of 5 kHz data from the inner and outer geophones.
– Inspect the realtime time series display in SignalExpress to ensure there were no spurious signals.
– Reject and repeat any experiments that were affected by: too early a spring release, the mass banging on its frame, excessive noise caused by hikers, wind gusts, vehicles, or mosquito attacks on the experimenters.
– Repeat six times in each configuration.

At each site four sets of six repeats were performed for clocked and anti-clocked cases, with either vertical or horizontal geophones installed. Additionally at the first site (Hverfjall) we performed four additional sets of six repeats with the inner and outer geophones swapped to ensure results were not an artifact of differing geophone responses. Due to fieldwork time constraints, this check could only be performed for Hverfjall. Table 1 summarises the experiments performed.

4 Analysis

Figure 6 shows example seismic records for single vertical and horizontal experiments. The advantage of using the mass on a double spring source is the that the signal has a single

Table 1 Summary of wind coupling experiments at Hverfjall and Holasandur. The mechanical noise source on the outer tripod was a brass sphere on a double spring in all cases. Column headings are: N number of repeats in each configuration; f_0 dominant frequency extracted from the seismograms; $\overline{T}$ mean transfer coefficient for each set of experiments with standard deviation $\sigma_{\overline{T}}$; $\widetilde{T}$ and $\sigma_{\widetilde{T}}$ are overall mean and standard deviation for each configuration. For Hverfjall $\sigma_{\widetilde{T}}$ is calculated from both geophone setups. For Holasandur $\sigma_{\widetilde{T}}$ includes an additional 15 % fractional error to account for differences caused by geophone response or tripod seating effects. Geophones are either vertical (1 and 2) or horizontal (3 and 4)

Site	Component	Orientation	Central geophone	N	f_0 (Hz)	$\overline{T}$	$\sigma_{\overline{T}}$	$\widetilde{T}$	$\sigma_{\widetilde{T}}$
Hverfjall	vertical	clocked	1	6	5.23	0.0192	0.00055		
Hverfjall	vertical	clocked	2	6	5.23	0.0219	0.00054	0.0205	0.00150
Hverfjall	vertical	anti-clocked	1	6	5.23	0.0164	0.00040		
Hverfjall	vertical	anti-clocked	2	6	5.23	0.0190	0.00025	0.0177	0.00142
Hverfjall	horizontal	clocked	3	6	4.32	0.0183	0.00090		
Hverfjall	horizontal	clocked	4	6	4.32	0.0215	0.00303	0.0199	0.00271
Hverfjall	horizontal	anti-clocked	3	6	4.32	0.0134	0.00076		
Hverfjall	horizontal	anti-clocked	4	6	4.32	0.0214	0.00391	0.0174	0.00498
Holasandur	vertical	clocked	2	6	5.28	0.0353	0.00108	0.0353	0.00540
Holasandur	vertical	anti-clocked	2	6	5.28	0.0321	0.00050	0.0321	0.00484
Holasandur	horizontal	clocked	4	6	4.43	0.0119	0.00069	0.0119	0.00191
Holasandur	horizontal	anti-clocked	4	6	4.43	0.0100	0.00031	0.0100	0.00153

well defined frequency that can be easily separated from the background noise. First, the trend was removed from each time series to remove DC bias. Second, a Hanning taper with a fractional width of 0.025 (i.e. a 0.75 s taper at each end) was applied to each time series to prevent discontinuities at the time series limits. Third, the time series was padded with zeros to a total length of four times the next power of two, giving a total time series length of 1048576 samples. Fourth, the time series were Fourier transformed into the spectral domain. The zero padding resulted in an interpolated spectral resolution of 0.00477 Hz, which improved the sampling of the spectral peak and made comparison of inner and outer tripod spectra more straightforward. Finally, the frequency f_0 and amplitude of the peaks associated with the mass on the double spring were extracted for both inner and outer tripod records. The ratio of the inner amplitude a_i to the outer amplitude a_o gave the transfer coefficient T between the WTS outer tripod and the SEIS inner tripod at frequency f_0. A mean transfer coefficient and standard deviation could then be determined for each set of repeat experiments.

Table 1 summarises the results from all experimental configurations and Fig. 7 represents these results graphically. At Hverfjall the results imply a value of $T \approx 0.02$ for both vertical and horizontal signals, with the anti-clocked tripod configuration having a slightly reduced value of T compared to the clocked configuration. Values of T determined when geophones 2 or 4 were on the inner tripod are typically ~ 15 % greater than those when geophones 1 or 3 were on the inner tripod. This difference could be due to different tripod seating between experiments or slightly differing geophone response and is included as an additional error source for the Holasandur experiments. At Holasandur the vertical and horizontal values for T are significantly different, taking values of $T \approx 0.035$ for the vertical and $T \approx 0.01$ for the horizontal. Again, the anti-clocked configuration has a slightly lower T value.
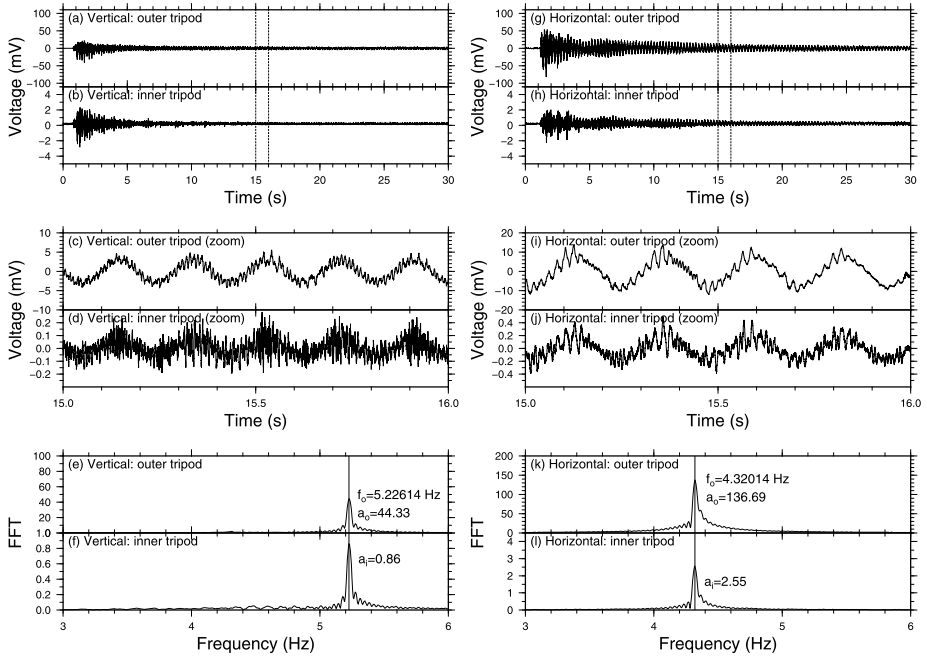
Fig. 6 Example seismic records. (**a**, **b**) Full 30 s time series from a single vertical component experiment measured on the outer and inner tripods. The records contain and initial one second pause before the spring is released, followed by large amplitudes immediately following spring release, and a subsequent gradual amplitude decrease due to the mass transferring energy to the tripod and regolith. (**c**, **d**) Zoom of the 15–16 s segment showing a single ~ 5 Hz sinusoidal signal, which is easily distinguishable from the noise. (**e**, **f**) Fourier transform after trend removal and tapering showing a single well-defined peak at f_0 with amplitudes a_o and a_i for the outer and inner tripod respectively. The WTS-to-SEIS transfer coefficient at f_0 is given by $T = a_i/a_o$. (**g**–**l**) Similar plots for a horizontal component example. Note the spring has a slightly lower resonant frequency when excited in the horizontal direction due to the reduced restoring force. In addition to the 5 Hz spring oscillator signal, the measured data also contain spurious high frequency signals ($\gtrsim 50$ Hz) from excitation of the tripods, nearby equipment, and geophone parasitic modes, which are not representative of the regolith transfer coefficient

5 Discussion

5.1 Wind Noise Transfer Coefficient

Our field experiments show that at 5 Hz the transfer coefficient T between the WTS and the SEIS tripod takes values in the range 0.01–0.04, with a mean value of 0.02. The vertical transfer coefficient ($T_v = 0.02$–0.04) was nominally higher than the horizontal transfer coefficient ($T_h = 0.01$–0.02).

For both sites the anti-clocked configuration has a slightly lower T value than the clocked configuration. This is to be expected as in the anti-clocked configuration the inner and outer tripod feet have greater separation. Smaller values of T mean less wind noise from the WTS is transferred to the seismometers. For InSight the anti-clocked configuration would thus be slightly preferable, although we regard the differences as so minimal that it should not be a stringent deployment requirement.

The variation between sites is approximately a factor of two for both vertical and horizontal components. The exact value of T for a particular site will depend upon the coupling of
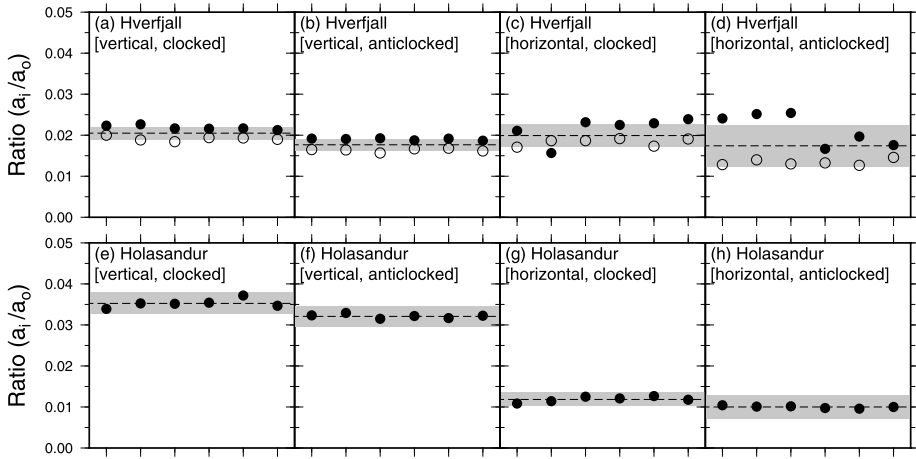
Fig. 7 Graphical summary of the measured transfer coefficients for all experiments. *Solid dots*, geophone 2 (vertical) or 4 (horizontal) on inner tripod. *Open dots*, geophone 1 (vertical) or 3 (horizontal) on inner tripod (Hverfjall only). *Dashed line* and *grey shading* indicate overall mean transfer coefficient $\widetilde{T}$ and standard deviation $\sigma_{\widetilde{T}}$ for each configuration. The results show that $\widetilde{T}$ takes values in the range 0.01–0.02 for the horizontal component and 0.02–0.04 for the vertical component. $\widetilde{T}$ has a slightly higher value in the clocked orientation

the tripod feet to the regolith and the propagation of seismic noise through the regolith. For unconsolidated surfaces, such as the fine grained basalt sand and loose tephra deposits used here, there are likely to be significant anelastic effects and variability. However, the Hverfjall site has a more Mars-like grain size distribution when compared to the Spirit rover's results (Cabrol et al. 2014) and may be more representative of conditions on Mars.

5.2 Comparison with Elastic Theory Predictions

Assuming ideal elastic behaviour, the ground displacement due to each WTS foot can be approximated as the displacement of an elastic half space acted upon by a circular flat-ended punch. For a load F applied to an elastic medium with Young's Modulus E and Poisson ratio ν, the displacement due a flat circular foot of radius a at distance r from the foot centre is given by (Sneddon 1946; Gladwell 1980; Maugis 2000):

$$d(r) = \frac{1 - \nu^2}{2E} \frac{F}{a} \quad \text{for: } r \leq a \tag{1}$$

$$d(r) = \frac{1 - \nu^2}{\pi E} \frac{F}{a} \sin^{-1}\left(\frac{a}{r}\right) \quad \text{for: } r > a \tag{2}$$

Here, as we are considering the transfer coefficient, only the relative variation of $d(r)$ is important and we can simply redefine $d(r)$ to refer to unit displacement of the elastic half space at the foot centre (i.e. changing the load, Young's Modulus and Poisson ratio in an elastic half space merely scales the displacement field, rather than changing its spatial distribution). In, which case:

$$d(r) = \frac{2}{\pi} \sin^{-1}\left(\frac{a}{r}\right) \tag{3}$$

where a is the radius of the anti-sink disc surrounding the foot and second order effects caused by the central spike have been ignored. The factor of $2/\pi$ is a normalisation factor to give a value of $d(r = a) = 1$. At the frequencies considered here (5 Hz) with a representative near surface seismic velocity of 500 ms^{-1} the wavelength of a seismic wave is of order 100 m. Therefore, the seismic signals generated at the WTS tripod ground contact can be considered in phase over both tripods and the displacements can be approximated using static-load Hertzian contact theory. We further assume that both tripods act as rigid bodies, which is reasonable at these low frequencies. Therefore, the total displacements D_j of the jth foot of the inner tripod are equal by symmetry and are given by the superposition of the displacement due to the three WTS tripod feet:

$$D_j = \frac{2}{\pi} \sum_{i=1}^{3} \sin^{-1}\left(\frac{a}{r_{ij}}\right) \quad \text{for: } j = 1 \ldots 3 \tag{4}$$

where r_{ij} is the distance between the centre of the ith outer tripod foot and the centre of the jth inner tripod foot. D_j is thus equal to the vertical transfer coefficient predicted by elastic theory T_e. Let the outer tripod have side length $2p$ and the inner tripod have length $2q$. For the clocked configuration, with inner foot j adjacent to outer foot i, simple trigonometry gives:

$$r_{i=j} = \frac{2}{\sqrt{3}}(p - q) \tag{5}$$

$$r_{i \neq j} = \sqrt{\frac{4}{3}(p^2 + pq + q^2)} \tag{6}$$

whereas for the anti-clocked configuration with inner foot j opposite outer foot i:

$$r_{i=j} = \frac{2}{\sqrt{3}}(p + q) \tag{7}$$

$$r_{i \neq j} = \sqrt{\frac{4}{3}(p^2 - pq + q^2)} \tag{8}$$

For our experiment $a = 0.03$ m, $p = 0.4$ m, and $q = 0.15$ m, which gives predicted vertical transfer coefficient $T_e = 0.134$ for a clocked inner tripod and $T_e = 0.125$ for an anti-clocked inner tripod.

Therefore, the vertical transfer coefficients predicted by elastic theory are 3–6 times larger than those measured in our experiments. This suggests anelastic effects are significant on unconsolidated surfaces at these frequencies. Fortunately the anelastic effect will act in our favour and will reduce wind noise coupled from the WTS by a similar factor, whereas the seismic signal from marsquakes or impacts will only be affected by approximately the square root of this factor as there is only the single set of contacts between the inner tripod and the regolith to consider.

Note that the relative differences between clocked and anti-clocked transfer coefficients predicted by elastic theory are similar to those measured in our experiment; a clocked to anti-clocked predicted ratio of 1.07 compared to a measured ratio of 1.13 ± 0.04 (average of vertical results in Table 1).

5.3 Estimates of Wind Noise due to Aerodynamic Lift

In Sect. 5.2 we showed that at short periods elastic theory does not provide a good approximation to the ground displacement of unconsolidated surfaces over extended distances; i.e.

outside the immediate vicinity of the foot. However, elastic theory can still be effectively used to model the foot displacement and is often applied in civil engineering and soil mechanics to estimate ground displacement when loads are applied to unconsolidated surfaces (Bowles 1996). Therefore, in this section we propagate a reasonable martian wind field though a hybrid noise coupling scheme, based on a combination of elastic theory ground deformation equations and our measured regolith transfer coefficient, in order to estimate a wind induced noise level.

We focus on the vertical noise component generated by short-period turbulent aerodynamic lift forces on the WTS. A full elastic theory treatment of the long period noise from wind induced forces on both WTS and lander is given in Murdoch et al. (2016a). Consider each WTS foot as a circular ended flat punch of radius a. From Maugis (2000), the downward displacement x relative to the WTS resting position is given by:

$$x = \frac{1 - v^2}{2E} \frac{W}{a} \qquad (9)$$

where W is the vertical external force applied to each foot, v is the Poisson ratio (0.25 for a standard linear solid), and E is the Young's modulus. Note that E is the *effective* Young's modulus of the bulk regolith, not the Young's modulus of individual grains, which will be orders of magnitude higher. Typical empirically derived values for sand and silt are $E = 2$–20 MPa with typical Poisson's ratios of 0.3–0.4 (Bowles 1996). Assuming symmetry, where the same force W is applied to each foot, gives a total vertical force applied to the outer tripod of $F = 3W$, with each foot having an identical displacement x. The equation of motion of the outer tripod is then:

$$F = m\ddot{x} + \mu\dot{x} + \frac{6aE}{1 - v^2}x \qquad (10)$$

where m is the WTS mass, $m\ddot{x}$ is the inertial force to accelerate the WTS, $\mu\dot{x}$ is the force caused by friction with friction parameter μ, $6aE/(1 - v^2)x$ is the total elastic force to deform the regolith by a distance x at each foot, and F is the external aerodynamic force applied to the WTS. Based on friction ratios measured in cone penetration tests, frictional forces are only a few percent of the total resistance force for typical soils and granular materials (Robertson 2009). Therefore, we assume that friction can be neglected, giving:

$$F \approx m\ddot{x} + \frac{6aE}{1 - v^2}x \qquad (11)$$

Equation (11) can be used to estimate the effective Young's modulus for our field sites. In our experiment the external force is supplied by the tension in the spring, which has a maximum of $F_{max} = 20 \pm 2$ N at the time of release. This force corresponds to a maximum velocity $\dot{x}_{max} = V_{max}/g$, where g is the geophone sensitivity at 5 Hz of 20 V/ms^{-1}, and V_{max} is the corresponding maximum voltage measured by the geophone on the outer tripod.

For the Hverfjall site $V_{max} = 36 \pm 17$ mV, which is equivalent to a maximum velocity of $\dot{x}_{max} = 1.8 \pm 0.8 \times 10^{-3}$ ms^{-1}. At 5 Hz, this corresponds to a maximum displacement of $x_{max} = 5.6 \pm 2.7 \times 10^{-5}$ m and a maximum acceleration of $\ddot{x}_{max} = 5.6 \pm 2.7 \times 10^{-2}$ ms^{-2}. Assuming $v = 0.35$, $F_{max} = 20$ N, $a = 0.03$ m, and $m = 7.4$ kg, implies an effective Young's modulus of $E = 1.7^{+1.6}_{-0.6}$ MPa. For the Holasandur site $V_{max} = 19 \pm 5$ mV, which is equivalent to $\dot{x}_{max} = 0.9 \pm 0.2 \times 10^{-3}$ ms^{-1}, $x_{max} = 3.0 \pm 0.7 \times 10^{-5}$ m, and $\ddot{x}_{max} = 2.9 \pm 0.7 \times 10^{-2}$ ms^{-2}, which implies an effective Young's modulus of $E = 3.3^{+1.1}_{-0.7}$ MPa. The values of E measured in our experiments have mean value of 2.5 MPa and span a 1-σ range of 1.1–4.4 MPa. These values are in agreement with literature values for the effective elastic modulus for sand and silt of $E = 2$–20 MPa (Bowles 1996).

Equation (11) can now be used to relate force applied to the WTS to ground displacement under the WTS feet. In the vertical direction, wind force is dominated by aerodynamic lift force F_L given by:

$$F_L = \frac{1}{2}\rho C_L A u^2 \tag{12}$$

where ρ is the atmospheric density, C_L is the lift coefficient, A is the WTS cross sectional area, and u is the wind speed. For the WTS $C_L = 0.36$ and $A = 0.209$ m^2 (Murdoch et al. 2016a). Mars has a typical atmospheric surface density of 0.02 kg m^{-3} (Seiff 1982), and a typical wind speed of 5–10 ms^{-1} (Hess et al. 1977), so these forces are of order 0.1 N or less.

To relate ground displacement to wind speed we use (11) and (12) to obtain the equation of motion of the WTS where aerodynamic lift is the external force:

$$m\ddot{x} = -\frac{1}{2}\rho C_L A u^2 - \frac{6aE}{1-v^2}x \tag{13}$$

For motion with a frequency f, the harmonic relation gives $\ddot{x} = \omega^2 x$, with $\omega = 2\pi f$. Therefore, for a turbulent wind flow with a spectral density of the squared amplitude $\langle U^2 \rangle$ (units m^2 s^{-2} Hz$^{-1/2}$), the ground displacement spectral density $\langle X \rangle$ (units m Hz$^{-1/2}$) is given by:

$$\langle X \rangle = \frac{\rho C_L A \langle U^2 \rangle}{8\pi^2 f^2 m + \frac{12aE}{1-v^2}} \tag{14}$$

The ground velocity and ground acceleration spectral densities are often more useful when considering noise and are given by $\langle \dot{X} \rangle = 2\pi f \langle X \rangle$ (units ms^{-1} Hz$^{-1/2}$) and $\langle \ddot{X} \rangle = 4\pi^2 f^2 \langle X \rangle$ (units ms^{-2} Hz$^{-1/2}$) respectively.

Unfortunately, no measurements of Mars surface winds are available at the ≥ 10 Hz sampling frequencies that would be required to define the turbulent wind spectra at 5 Hz. Therefore, amplitude spectral densities are based on extrapolations from the Viking and Phoenix Lander wind sensor data obtained at mast heights of 1.6 m. Following the extrapolation of Murdoch et al. (2016a) we use a squared amplitude spectral density $\langle U^2 \rangle$ (m^2 s^{-2} Hz$^{-1/2}$) for a typical day-time wind regime of:

$$\langle U^2 \rangle = B \left(\frac{\ln z - \ln z_0}{\ln z_{\text{ref}} - \ln z_0} \right)^2 \left(\frac{f}{f_{\text{cut}}} \right)^{-5/3} \tag{15}$$

where $B = 125$ m^2 s^{-2} Hz$^{-1/2}$, $f_{\text{cut}} = 0.015$ Hz, z is the height above the surface (0.4 m for the WTS), z_0 is the aerodynamic roughness length (Greeley and Iversen 1985), $z_{\text{ref}} = 1.6$ m is the reference height, and the $-5/3$ power is the classic Kolmogorov turbulent spectral dependence. This expression is only valid for frequencies greater than f_{cut}.

Equations (14) and (15) can now be used to estimate the wind noise from aerodynamic lift on the WTS. The two remaining critical parameters are z_0 and E for the InSight landing site, both of which contain considerable uncertainty.

A value of $z_0 = 3$ cm for Mars has been estimated from wind profile data measured by windsocks at the Pathfinder landing site (Sullivan et al. 2000). However, the Pathfinder site is considerably rougher than the InSight landing site. Therefore, we use a value of $z_0 = 1$ cm, which lies at the upper end of estimates by Sutton et al. (1978), with a conservative factor of three error estimate to cover the range in reported values.

The effective regolith Young's modulus E has not been directly measured for Mars. For context, E has been measured in the laboratory for lunar regolith simulant JSC-1A by Alshibli and Hasan (2009), who obtained values of 11.1–46.7 MPa for confining pressures in the

range 10–200 kPa. For a WTS tripod mass of $m = 9.5$ kg and a foot radius of $a = 0.03$ m, the pressure applied by each foot under Mars gravity is $P = mg/(3\pi a^2) = 4.2$ kPa. Using a log-log linear fit to the data in Alshibli and Hasan (2009) gives an extrapolated value of $E \sim 7$ MPa at these pressures—comparable, but somewhat higher, than our field derived values. Here we prefer to use the value of $E = 2.5$ MPa from our analogue field measurements, but include a factor of four error to cover the uncertainties.

For our nominal noise case we assume a central frequency of $f_0 = 5$ Hz, a roughness length of $z_0 = 0.01$ m, an effective ground Young's modulus of $E = 2.5$ MPa, and a Poisson ratio of 0.35. The resulting ground acceleration noise spectral density directly under the WTS feet is 6×10^{-9} ms^{-2} Hz$^{-1/2}$, with a range of $1–30 \times 10^{-9}$ ms^{-2} Hz$^{-1/2}$ once uncertainties in z_0 and E are included. Therefore, the vertical regolith transfer coefficient $T = 0.02–0.04$ results in a nominal noise level measured on the inner SEIS tripod of 2×10^{-10} ms^{-2} Hz$^{-1/2}$, with an uncertainty range of $0.2–12 \times 10^{-10}$ ms^{-2}Hz$^{-1/2}$. This is at least an order of magnitude less than the SEIS-SP noise specification of 10^{-8} ms^{-2} Hz$^{-1/2}$, even for the most pessimistic case. Therefore, at short periods we expect wind noise due to aerodynamic lift of the WTS to be much less than the instrument noise.

Longer period noise sources are considered by Murdoch et al. (2016a) using an elastic theory approach, including aerodynamic lift, aerodynamic drag, and transmission of lander solar panel vibration modes through the regolith. For comparison, Murdoch et al. (2016a)'s elastic theory model of the WTS vertical noise gives $\lesssim 2.5 \times 10^{-10}$ ms^{-2} Hz$^{-1/2}$ at 1 Hz. Extrapolating these results to 5 Hz suggests $\lesssim 4 \times 10^{-10}$ ms^{-2} Hz$^{-1/2}$, which is consistent with our nominal value of 2×10^{-10} ms^{-2} Hz$^{-1/2}$ when a reduction factor of 3–6 to account for the anelastic effect is applied. Further environmental noise sources and instrument noise is discussed in detail by Mimoun et al. (2016) and Murdoch et al. (2016a,b).

6 Conclusions

We performed a series of analogue field experiments using a simplified scale model of the InSight SEIS experiment to determine the transfer coefficient between the Wind and Thermal Shield (WTS) and the SEIS instrument package seismometers. Using two field locations in Iceland we determined the transfer coefficient at 5 Hz to be 0.02–0.04 for the vertical component and 0.01–0.02 for the horizontal component. These values are 3–6 times less than the transfer coefficient predicted using elastic theory and imply that at short periods there is a significant anelastic component to regolith behaviour. There was a weak dependence of transfer coefficient on the relative orientation of the WTS and SEIS tripods, with the anticlocked orientation having slightly smaller transfer coefficients than the clocked orientation. However, the difference is so small that this does not constitute an important deployment requirement.

Anelastic regolith response at short periods implies that noise originating from wind-induced vibrations will be much smaller than predicted by conventional elastic theory, and will thus result in a higher signal-to-noise for seismic events once deployed on Mars' surface. The effect of wind turbulence induced aerodynamic lift on the vertical noise component was considered and was found to be $0.2–12 \times 10^{-10}$ ms^{-2} Hz$^{-1/2}$ (nominally 2×10^{-10} ms^{-2} Hz$^{-1/2}$), for a reasonable martian wind turbulence spectrum and range of surface properties. This is an order of magnitude below the SEIS-SP noise specification and is not predicted to be a significant noise source. At longer periods (< 1 Hz), anelastic effects are expected to be smaller.

References

K.A. Alshibli, A. Hasan, Strength properties of JSC-1A lunar regolith simulant. J. Geotech. Geoenviron. Eng. **135**, 673–679 (2009)

O. Arnalds, F.O. Gisladottir, H. Sigurjonsson, Sandy deserts of Iceland: an overview. J. Arid Environ. **47**, 359–371 (2001)

R.E. Arvidson, R.C. Anderson, P. Bartlett, J.F. Bell, P.R. Christensen, P. Chu, K. Davis, B.L. Ehlmann, M.P. Golombek, S. Gorevan, E.A. Guinness, A.F.C. Haldemann, K.E. Herkenhoff, G. Landis, R. Li, R. Lindemann, D.W. Ming, T. Myrick, T. Parker, L. Richter, F.P. Seelos, L.A. Soderblom, S.W. Squyres, R.J. Sullivan, J. Wilson, Localization and physical property experiments conducted by Opportunity at Meridiani Planum. Science **306**, 1730–1733 (2004)

W.B. Banerdt, S. Smrekar, L. Alkalai, T. Hoffman, R. Warwick, K. Hurst, W. Folkner, P. Lognonné, T. Spohn, S. Asmar, D. Banfield, L. Boschi, U. Christensen, V. Dehant, D. Giardini, W. Goetz, M. Golombek, M. Grott, T. Hudson, C. Johnson, G. Kargl, N. Kobayashi, J. Maki, D. Mimoun, A. Mocquet, P. Morgan, M. Panning, W.T. Pike, J. Tromp, T. van Zoest, R. Weber, M. Wieczorek, Insight Team, InSight: an integrated exploration of the interior of Mars, in *Lunar and Planetary Science Conference*. Lunar and Planetary Inst. Technical Report, vol. 43, 2012, p. 2838

W.B. Banerdt, S. Smrekar, P. Lognonné, T. Spohn, S.W. Asmar, D. Banfield, L. Boschi, U. Christensen, V. Dehant, W. Folkner, D. Giardini, W. Goetze, M. Golombek, M. Grott, T. Hudson, C. Johnson, G. Kargl, N. Kobayashi, J. Maki, D. Mimoun, A. Mocquet, P. Morgan, M. Panning, W.T. Pike, J. Tromp, T. van Zoest, R. Weber, M.A. Wieczorek, R. Garcia, K. Hurst, InSight: a discovery mission to explore the interior of Mars, in *Lunar and Planetary Science Conference*. Lunar and Planetary Inst. Technical Report, vol. 44, 2013, p. 1915

N. Barlow, *Mars: An Introduction to Its Interior, Surface and Atmosphere* (Cambridge Univ. Press, Cambridge, 2008)

J.E. Bowles, *Foundation Analysis and Design*, 5th edn. (McGraw-Hill, New York, 1996)

N.A. Cabrol, K. Herkenhoff, A.H. Knoll, J. Farmer, R. Arvidson, E. Grin, R. Li, L. Fenton, B. Cohen, J.F. Bell, R. Aileen Yingst, Sands at Gusev Crater, Mars. J. Geophys. Res. **119**, 941–967 (2014). doi:10.1002/2013JE004535

P.R. Christensen, H.J. Moore, The Martian surface layer, in *Space Science Series*, ed. by H.H. Kieffer, B.M. Jakosky, C.W. Snyder, M.S. Matthews (University of Arizona Press, Tucson, 1992), pp. 686–729

P.-A. Dandonneau, P. Lognonne, W.B. Banerdt, S. Deraucourt, T. Gabsi, J. Gagnepain-Beyneix, T. Nebut, O. Robert, S. Tillier, K. Hurst, D. Mimoun, U. Christensen, M. Bierwirth, R. Roll, T. Pike, S. Calcutt, D. Giardini, D. Mance, P. Zweifel, P. Laudet, L. Kerjean, R. Perez, Seis Team, The SEIS InSight VBB experiment, in *Lunar and Planetary Science Conference*. Lunar and Planetary Inst. Technical Report, vol. 44, 2013, p. 2006

P.M. Davis, Meteoroid impacts as seismic sources on Mars. Icarus **105**, 469–478 (1993)

A.K. Delahunty, W.T. Pike, Metal-armouring for shock protection of MEMS. Sens. Actuators A, Phys. **215**, 36–43 (2014)

G.M.L. Gladwell, *Contact Problems in the Classical Theory of Elasticity*. Monographs and Textbooks on Mechanics of Solids and Fluids (Springer, Netherlands, 1980)

M.P. Golombek, W.B. Banerdt, K.L. Tanaka, D.M. Tralli, A prediction of Mars seismicity from surface faulting. Science **258**, 979–981 (1992)

R. Greeley, J.D. Iversen, *Wind as a Geological Process on Earth, Mars, Venus and Titan*. Cambridge Planetary Science Series vol. 4 (Cambridge Univ. Press, Cambridge, 1985)

R. Greeley, N.T. Bridges, R.O. Kuzmin, J.E. Laity, Terrestrial analogs to wind-related features at the Viking and Pathfinder landing sites on Mars. J. Geophys. Res. **107**(E1), 5005 (2002). doi:10.1029/2000JE001481

W.K. Hartmann, T. Thorsteinsson, F. Sigurdsson, Martian hillside gullies and Icelandic analogs. Icarus **162**, 259–277 (2003)

S.L. Hess, R.M. Henry, C.B. Leovy, J.E. Tillman, J.A. Ryan, Meteorological results from the surface of Mars—Viking 1 and 2. J. Geophys. Res. **82**, 4559–4574 (1977)

M. Knapmeyer, J. Oberst, E. Hauber, M. Wahlisch, C. Deuchler, R. Wagner, Working models for spatial distribution and level of Mars' seismicity. J. Geophys. Res. **111**, 11006 (2006)

P. Lognonne, J.G. Beyneix, W.B. Banerdt, S. Cacho, J.F. Karczewski, M. Morand, Ultra broad band seismology on InterMarsNet. Planet. Space Sci. **44**, 1237–1249 (1996)

P. Lognonne, W. Banerdt, T. Pike, D. Giardini, U. Christensen, D. Banfield, D. Mimoun, P. Laudet, S. de Raucourt, M. Bierwirth, P. Zweifel, S. Calcutt, K. Hurst, C. Bruce, SEIS/InSight and Mars seismology: development status and focus on the impact detection, in *EGU General Assembly Conference Abstracts*. EGU General Assembly Conference Abstracts, vol. 16, 2014, p. 12183

P. Lognonne, W.B. Banerdt, R.C. Weber, D. Giardini, W.T. Pike, U. Christensen, D. Mimoun, J. Clinton, V. Dehant, R. Garcia, C.L. Johnson, N. Kobayashi, B. Knapmeyer-Endrun, A. Mocquet, M. Panning, S. Smrekar, J. Tromp, M. Wieczorek, E. Beucler, M. Drilleau, T. Kawamura, S. Kedar, N. Murdoch, P. Laudet, InSight/SEIS Team, Science goals of SEIS, the InSight seismometer package, in *Lunar and Planetary Science Conference*. Lunar and Planetary Inst. Technical Report, vol. 46, 2015, p. 2272

R.D. Lorenz, J.R. Zimbelman, *Dune Worlds* (Springer, Heidelberg, 2014)

H.B. Mattsson, Á. Höskuldsson, Contemporaneous phreatomagmatic and effusive activity along the Hverfjall eruptive fissure, north Iceland: eruption chronology and resulting deposits. J. Volcanol. Geotherm. Res. **201**, 241–252 (2011)

D. Maugis, *Contact, Adhesion, and Rupture of Elastic Solids* (Springer, Berlin, 2000)

D. Mimoun, P. Lognonné, W.B. Banerdt, K. Hurst, S. Deraucourt, J. Gagnepain-Beyneix, T. Pike, S. Calcutt, M. Bierwirth, R. Roll, P. Zweifel, D. Mance, O. Robert, T. Nébut, S. Tillier, P. Laudet, L. Kerjean, R. Perez, D. Giardini, U. Christenssen, R. Garcia, The InSight SEIS experiment, in *Lunar and Planetary Science Conference*. Lunar and Planetary Inst. Technical Report, vol. 43, 2012, p. 1493

D. Mimoun, M. Murdoch, P. Lognonné, K. Hurst, T. Pike, W.B. Banerdt, The Mars seismic noise model of the InSight mission. Space Sci. Rev. (2016, this issue)

N. Murdoch, D. Mimoun, R. Garcia, W. Rappin, T. Kamamura, P. Lognonné, Evaluating the wind-induced mechanical noise on the InSight seismometers. Space Sci. Rev. (2016a, this issue). doi:10.1007/s11214-016-0311-y

N. Murdoch, B. Kenda, T. Kawamura, A. Spiga, P. Lognonné, D. Mimoun, W.B. Banerdt, Estimations of the seismic pressure noise on Mars determined from Large Eddy Simulations and demonstration of pressure decorrelation techniques for the InSight mission. Space Sci. Rev. (2016b, this issue)

M.P. Panning, Planned products of the Mars structure service for the InSight mission to Mars. Space Sci. Rev. (2016)

W.T. Pike, I.M. Standley, W.B. Banerdt, A high-sensitivity broad-band seismic sensor for shallow seismic sounding of the lunar regolith, in *36th Annual Lunar and Planetary Science Conference*, ed. by S. Mackwell, E. Stansbery. Lunar and Planetary Inst. Technical Report, vol. 36, 2005, p. 2002

W.T. Pike, U. Staufer, M.H. Hecht, W. Goetz, D. Parrat, H. Sykulska-Lawrence, S. Vijendran, M.B. Madsen, Quantification of the dry history of the Martian soil inferred from in situ microscopy. Geophys. Res. Lett. **38**, 24201 (2011). doi:10.1029/2011GL049896

G.P. Roberts, B. Matthews, C. Bristow, L. Guerrieri, J. Vetterlein, Possible evidence of paleomarsquakes from fallen boulder populations, Cerberus Fossae, Mars. J. Geophys. Res. **117**(E2), 003816 (2012)

P.K. Robertson, Interpretation of cone penetrations tests—a unified approach. Can. Geotech. J. **46**, 1337–1355 (2009)

S.W. Ruff, P.R. Christensen, Bright and dark regions on Mars: particle size and mineralogical characteristics based on thermal emission spectrometer data. J. Geophys. Res. **107**, 5127 (2002). doi:10.1029/2001JE001580

A. Seiff, Post-Viking models for the structure of the summer atmosphere of Mars. Adv. Space Res. **2**, 3–17 (1982)

I.N. Sneddon, Boussinesq's problem for a flat-ended cylinder. Proc. Camb. Philol. Soc. **42**, 29–39 (1946)

R. Sullivan, R. Greeley, M. Kraft, G. Wilson, M. Golombek, K. Herkenhoff, J. Murphy, P. Smith, Results of the Imager for Mars Pathfinder windsock experiment. J. Geophys. Res. **105**, 24547–24562 (2000)

J.L. Sutton, C.B. Levoy, J.E. Tillman, Diurnal variations of the Martian surface layer meteorological parameters during the first 45 sols at two Viking Lander sites. J. Atmos. Sci. **35**, 2346–2355 (1978)

J. Taylor, Seismic exploration of Mars and the NASA InSight mission, PhD thesis, University of Bristol, 2014

J. Taylor, N.A. Teanby, J. Wookey, Estimates of seismic activity in the Cerberus Fossae region of Mars. J. Geophys. Res. **E118**, 2570–2581 (2013)

N.A. Teanby, Predicted detection rates of regional-scale meteorite impacts on Mars with the InSight short-period seismometer. Icarus **256**, 49–62 (2015)

N.A. Teanby, J. Wookey, Seismic detection of meteorite impacts on Mars. Phys. Earth Planet. Inter. **186**, 70–80 (2011)